

SO-NeRF: Active View Planning for NeRF using Surrogate Objectives

Keifer Lee¹, Shubham Gupta¹, Sungyoung Kim^{1,2}, Bhargav Makwana^{1,2},
Chao Chen¹, Chen Feng^{1,*}

¹New York University ²Denotes Equal Contribution

<https://ai4ce.github.io/SO-NeRF>

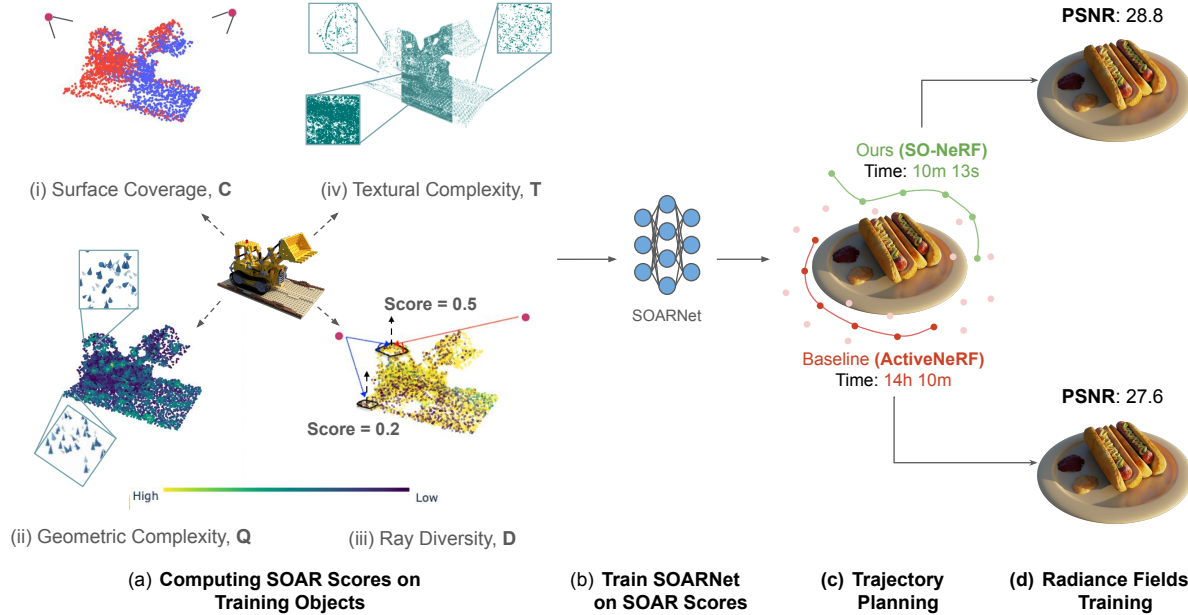


Figure 1. **Overview** of SO-NeRF against a baseline, ActiveNeRF [33]. (a) Given any training mesh, we compute the individual surrogate objective scores **C**, **Q**, **D** and **T**, (b) train a model, SOARNet (c) for trajectory planning, without the need of prior visit of the candidate poses (unlike ActiveNeRF). (d) We can achieve comparable NeRF quality, but with a significant speed-up compared to the baseline.

Abstract

Despite the great success of Neural Radiance Fields (NeRF), its data-gathering process remains vague with only a general rule of thumb of “sampling as densely as possible”. The lack of understanding of what actually constitutes good views for NeRF makes it difficult to actively plan a sequence of views that yield the maximal reconstruction quality. We propose Surrogate Objectives for Active Radiance Fields (SOAR), which is a set of interpretable functions that evaluates the goodness of views using geometric and photometric visual cues - surface coverage, geometric complexity, textural complexity, and ray diversity. Moreover, by learning to infer the SOAR scores from a deep network, SOARNet, we are able to effectively select views in mere

seconds instead of hours, without the need for prior visits to all the candidate views or training any radiance field during such planning. Our experiments show SOARNet outperforms the baselines with $\sim 80x$ speed-up while achieving better or comparable reconstruction qualities. We finally show that SOAR is model-agnostic, thus it generalizes across fully neural-implicit to fully explicit approaches.

1. Introduction

A key aspect of a practical and intelligent embodied agent is the ability to dynamically respond and plan appropriately to an ever-changing environment - dubbed active perception [2]. Of course, one presupposes the ability to construct a reliable representation of the environment as a prior, and a class of approach has been found to be particularly efficacious in recent years - neural implicit representations

*The work is supported by NSF Awards 2238968 and 2322242. The corresponding author is Chen Feng cfeng@nyu.edu

with Neural Radiance Fields (NeRF) [1, 29]. Its applications range from Virtual Reality [8, 26, 44] to Simultaneous Localization, Mapping (SLAM) [20, 38, 50].

However, in contrast to their popularity, the prototypical process of constructing such representations remained vague with a general rule of thumb - capture as many images of the subject as densely and directionally varied as possible. The latter suggestion may be fine for one-off tasks or small subjects, but grows to be intractable when either of the aforementioned conditions are not satisfied; e.g. capturing images for thousands of products or trying to reconstruct the Santa Maria del Fiore in its entirety for large-scale exploration and neural topological mapping. In robotics context, a properly perceived representation is key to planning and navigation. Therefore, it is of interest to study more efficient ways of capturing the required images, and indeed this is known as the Next Best View (NBV) problem [34].

There have been many proposed approaches to tackle the NBV problem in the classical Structure from Motion (SfM) setting [14, 16], and even in the recent neural implicit framework [5, 13, 19, 21, 33, 35, 45]. However, these methods so far suffer from some key problems from an application-viability perspective in one way or another. Probabilistic uncertainty estimation methods such as ActiveNeRF [33], NeurAR [35] and Bayes' Rays [13] are either too slow or not straightforward to work with by requiring training of a NeRF model - effectively an in-flight or post hoc approach; they are also not interpretable as abstract probabilistic uncertainties does not correspond to actual physical qualities. On the other end of the spectrum, there are methods from classical SfM tasks such as SCONE [14] that utilizes intuitive concepts like surface coverage as a proxy objective to maximize for. However, these unidimensional methods are too simplistic, which may not generalize well across object classes with different structure.

Therefore, in this work, we introduce SOAR to tackle the aforementioned problems of active perception for radiance fields models such as NeRF. Specifically, the main contributions of our work are as follows:

1. We propose a set of surrogate objectives, SOAR to characterize informative samples for training radiance fields models. These functions correspond directly to physical qualities, rendering them intuitive and explainable.
2. Unlike in-flight and post hoc methods, SOAR is prescriptive, not needing any radiance field model training at all. Therefore it is also radiance fields model-agnostic.
3. We further devised a method to efficiently compute these objectives with a novel neural network, dubbed SOAR-Net, generating trajectories in seconds instead of hours.
4. Finally, SOAR provides an alternative training-free approach to estimating the goodness of a radiance field model with respect to the input data. We will release our code and data for reproducibility.

2. Related Work

Novel View Synthesis is generating views of the given object or scene from previously unseen camera poses. This is a challenging task due to the high uncertainty of elements that were previously occluded from the field of view [27, 28, 46, 49]. While there are many approaches recently published [4, 22, 43, 47], we only explore Novel View Synthesis using radiance fields [11, 29] to stay within the scope of this paper. Note that the original NeRF [29] by Mildenhall et al. shall be referenced as *Vanilla NeRF* interchangeably henceforth to distinct the generic idea of neural radiance field modeling and the actual model itself.

The original NeRF while impressive was not very computationally efficient as it encodes the object via a neural network (implicit representation). To further improve the run-time performance, there have been recent works alleviating the computation bottleneck [12], and these works can be categorized as baked (fully-implicit), hybrid, and fully-explicit representation methods [6, 10, 18, 30]. Fridovich-Keil et al. [10] voxelize the scene and store the density and spherical harmonics coefficients as scalars and vectors per color channel respectively. As such, slow neural networks are not required, resulting in what's known as a fully-explicit representation. Müller et al. [30] leveraged a multi-resolution hash table of feature vectors to lookup the pixel's features, resulting in a massive speed-up. Since their approach leverages a neural network for volumetric rendering, such methods are classified as hybrid representation approaches. In the same class, Chen et al. [6] proposed a method with massive speed-up and saving in memory footprint compared to fully-explicit approaches by representing a scene as a 4D tensor and decomposing the tensor into multiple low-rank components.

Next Best View planning is a highly relevant topic for robotic perception that deals with finding the best sensor positioning to maximize information gain. This also directly ties in with the idea of active perception [2, 3], where the observer moves around a scene with an intention to better capture salient information. Active perception has previously been employed for various tasks [31, 37, 41] but only recently for training radiance fields model [33].

Guédon et al. [14] propose a hybrid method that predicts an occupancy grid so as to maximize the total surface coverage using a neural networks and Monte Carlo integration over a volumetric representation. Improving on that, [16] utilizes only camera inputs and is able learn in a self-supervised fashion. Kopanas and Drettakis [24] introduced observation frequency and angular uniformity as metrics to improve convergence for free-viewpoint navigation. Dhama et al. [9] propose a two-stage process that predicts the complete point cloud using partial observations and selects for views that minimizes the distance traveled.

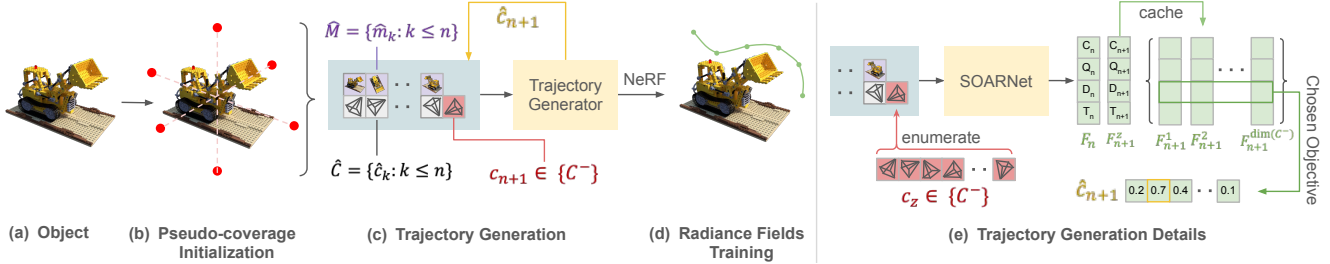


Figure 2. The overall pipeline of our proposed approach. (a) Given an object, (b) we initialize via pseudo-coverage initialization to obtain a set of starting poses $\hat{\mathcal{M}}$ and corresponding camera-poses $\hat{\mathcal{C}}$. (c) We then generate a trajectory for sampling in a greedy manner by computing the objective scores of all unseen camera-poses, c_{n+1} where \mathcal{C}^- is the set of all unseen camera-poses. (e) To compute said scores, we utilize our novel model, SOARNet for speedy inference, and we then simply pick the candidate with the highest score, c_z as our next pose, \hat{c}_{n+1} until we reach our budget, \mathcal{B} for (d) radiance fields training.

Uncertainty estimation in NeRF has recently received a lot of interest. Pan et al. [33] incorporates uncertainty estimation into the Vanilla NeRF training pipeline, which learns to estimate the uncertainty of candidate poses in parallel during training via Bayesian estimation. These candidates are then greedily selected post-training to maximize the estimated information gain. Lee et al. [25] proposes a ray-based uncertainty estimator by computing the entropy of the distribution of the color samples along each ray. Similarly, Shen et al. [39] presents a generalized NeRF model that can learn the probability distribution of all radiance fields representing a given scene for uncertainty estimation via Bayesian learning. Jin et al. [21] proposes a generic framework that learns to predict the uncertainty of each candidate poses, but without needing to train a radiance fields model. However, to compute the uncertainties, their method still requires the images taken from said candidate poses in the first place, which is a non-negligible limitation in real-world applications.

Goli et al. [13] presents a post hoc framework to evaluate the uncertainty in any pretrained NeRF model. The framework produces a spatial uncertainty field by introducing perturbations along the learned camera rays and by utilizing Bayesian Laplace approximations. Ran et al. [35] proposes a proxy for the Peak Signal-to-Noise Ratio (PSNR) metric that is jointly trained with the parameters of an implicit radiance fields model to predict a new quantity, dubbed Neural Uncertainty for trajectory planning. Our approach, does not perform post-hoc uncertainty estimation, but preemptively evaluates unseen candidate poses via the SOAR scores.

3. Methodology

We begin by formulating the problem - given an object and a corresponding set of images of said object, $\mathcal{M} = \{m_1, m_2, \dots, m_N\}$, taken from camera-poses, $\mathcal{C} = \{c_1, c_2, \dots, c_N\}$, $c \in \mathbb{R}^{3 \times 4}$ and a budget constraint, $\mathcal{B} \in \mathbb{N}$ we want to select a subset of poses, subjected to the con-

straint, that will maximize a reconstruction quality metric such as PSNR, Γ via a radiance fields model, Ω . Formally,

$$\hat{\mathcal{C}} = \arg \max_c \Gamma(\Omega(\mathcal{C}, \mathcal{M})) \quad s.t. \quad \dim(\hat{\mathcal{C}}) = \mathcal{B} \quad (1)$$

In the following subsections, we outline the different parts of the pipeline. In 3.1, we formally define the objective functions of our approach from first principles. In 3.2, we introduce SOARNet which enables us to efficiently compute the objective scores. Lastly, in 3.3 we introduce the finalized framework by delineating a simple trajectory planning schema with SOARNet.

3.1. Objective Functions Definitions

We begin with a set of presuppositions on the qualities of a training set that would yield a NeRF with good reconstruction as measured via Γ . Fundamentally, we hypothesized from first principles that a good training set can be obtained by maximizing the surface coverage of the object, the attention paid to local regions with particular geometric or textural complexity, and the resulting multi-view diversity of observations. Succinctly, we refer to the aforementioned qualities as the (i) Surface Coverage, \mathbf{C} (ii) Geometric Complexity, \mathbf{Q} (iii) Textural Complexity, \mathbf{T} (iv) and Ray Diversity, \mathbf{D} respectively.

Surface Coverage, \mathbf{C} as defined is simply the ratio of seen faces, j via the image taken from the k -th camera-pose, c_k , against the total number of faces of the object or mesh, J . We can therefore define a corresponding objective function for \mathbf{C} as follows, where $f_C \in \mathbb{R}$

$$f_C = \frac{1}{J} \sum_j U\left(\sum_k V_j^k\right) \quad (2)$$

where $U(\cdot)$ is the Heaviside step function, n is the total number of camera-poses visited, and V_j^k is an indicator function corresponding to the visibility of face j from the

k -th camera-pose. Given the mesh of an object, optimizing for Eq. (2) amounts to maximizing the number of unique faces seen across the camera-poses.

Geometric Complexity, Q corresponds to the variability of the mesh faces’ configurations, and one way to quantify this complexity is via the mesh normals, \hat{n} . For example, a geometrically complex mesh such as a cathedral, would have a higher degree of surface normal variability compared to a simple smooth ball due to the varied substructures comprising the cathedral - e.g. pillars, the dome. In the case of the cathedral, we would intuitively want to pay extra attention to the local regions that are complex by sampling more varied views of said regions.

We formally define the objective function for **Q** as follows, where $f_Q \in \mathbb{R}$

$$f'_Q = |\text{LoG}(\hat{n}_j; \sigma_Q)| \beta_Q V_j^k + 1 \quad (3)$$

$$f_Q = \frac{1}{J(5\sigma_Q)^2} \sum_j^J f'_Q \quad (4)$$

where $\text{LoG}(\cdot)$ is the Laplacian of Gaussian filter, σ_Q is the standard deviation of the Gaussian filter, β_Q a scaling factor, f'_Q is the per-face geometric complexity and f_Q is the normalized total complexity. We take the absolute value of the output since the directionality of the normal variations does not matter. Maximization of Eq. 4 will encourage the selection of camera-poses with higher geometric complexity as defined above. In practice, a scaling discount factor, d_Q is applied towards the **Q** values of overlapping faces seen during trajectory planning in order to control for over-emphasis on certain local regions with unusually high geometric complexity, trapping it in a local maxima.

Textural Complexity, T corresponds to the photometric variation of images taken at camera-pose, c_k of the object. This means that **T** is computed with respect to the 2D projections of the object instead of the underlying 3D mesh. We have chosen this simplified approach for **T** since unlike geometric complexities which may be hard to discern on 2D projections, textural characteristics are not. Similar to Geometric Complexity, **Q** we hypothesized that regions with high textural complexity should be paid extra attention. Formally, we define the corresponding objective function for **T** as follows, where $f_T \in \mathbb{R}$

$$f'_T = \text{Hist}(\text{LBP}(m_k; r_T, p_T)) \quad (5)$$

$$f_T = 1 - f'_T[b] \quad (6)$$

where $\text{Hist}(\cdot)$ is simply the histogram function, b the last bin’s index, $\text{LBP}(\cdot)$ is the Local Binary Pattern texture descriptor [32], r_T and p_T are the filter radius and the

number of circularly symmetric local neighborhood points of the descriptor, and finally m_k is the image taken at camera-pose, c_k . Similar to f_Q , in practice, we also impose a discount factor, d_T towards the **T** values seen during trajectory planning to prevent overfitting, and we used r_T of 3 and p_T of 3. Finally, we compute the final score by averaging f_T computed on the Hue and Saturation channels of the image respectively. Maximization of Eq. (6) is equivalent to selecting the image with the highest textural complexity.

Ray Diversity, D as defined is the variation of the rays, i projected from various viewing poses observing a particular face, j of the object mesh. Intuitively, having highly varied novel views of the object faces would yield better reconstruction. The idea is closely related to densely sampling a set of training images from as many views as possible to improve multi-view correspondences. We went a step further here by exactly quantifying said idea with a formal definition of the objective function as follows

$$\theta_{ij}^k = \left| \frac{180^\circ}{\pi} \arccos \left(\frac{i \hat{n}_j}{|i| |\hat{n}_j|} \right) \right| - 90^\circ \quad (7)$$

where θ_{ij}^k is the augmented ray-surface grazing angle between ray i from camera-pose c_k and face j with surface normal \hat{n}_j . However, as opposed to indiscriminately maximizing for view-angle variance, we impose a penalty towards any ray observing a face beyond a certain grazing angle via soft-thresholding. The intuition behind the penalty is derived from the observation that it becomes increasingly difficult to visually obtain useful information about a given object’s face as we approach the orthogonal angle of its surface normal. We perform said soft-thresholding by assigning each observing ray, i with an outlier score

$$\psi_{ij}^k = 1 - \frac{\alpha_1}{1 + e^{-\theta_{ij}^k + \alpha_2}} \quad (8)$$

where ψ_{ij}^k is the outlier score, and α_1 and α_2 are hyper-parameters to control the grazing angle soft-threshold with values of 1 and -10 respectively. We then compute the total outlier ratio of face j as follows

$$\phi_j = \frac{1}{K_j} \sum_k^n \left(\sum_i^I \psi_{ij}^k V_{ij}^k \right) \quad (9)$$

where

$$K_j = \sum_k^n \sum_i^I V_{ij}^k \quad (10)$$

which simplifies Eq. (9)

$$\phi_j = \mathbb{E}[\psi_{ij}^k] \quad (11)$$

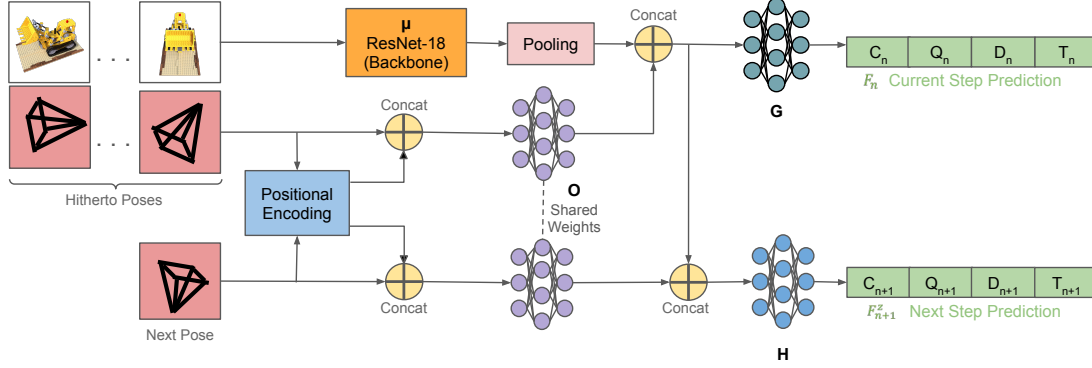


Figure 3. Architecture of the SOARNet.

Next, we compute the ray diversity, d_j of face j as follows

$$\delta_j = \frac{1}{I^3} \left[\sum_i^I (x_i - \bar{x}_i)^2 \sum_i^I (y_i - \bar{y}_i)^2 \sum_i^I (z_i - \bar{z}_i)^2 \right] \quad (12)$$

where x, y, z are the corresponding principal axis values of each observing ray i . This is akin to multiplying the variances of each individual principal axis of the observing rays.

$$\delta_j = \sigma_x^2 \sigma_y^2 \sigma_z^2 \quad (13)$$

Finally, the normalized effective Ray Diversity objective function is as follows, where $f_D \in \mathbb{R}$

$$f_D = \frac{1}{J} \sum_j^J \delta_j \phi_j \quad (14)$$

Note that for all the objective functions of f_C, f_Q, f_D , and f_T , their values are further smoothed and clipped with the following smoothing function, $\xi: \mathbb{R} \mapsto [0, 1]$ with α_3 of 3.

$$\xi(x) = \max \left(\min \left(\frac{1}{1 + [e^{(-\alpha_3 e x) + (\alpha_3 0.5 e)}]}, 1 \right), 0 \right) \quad (15)$$

3.2. Efficient Computation with SOARNet

With the objective functions defined, we now turn our attention to efficient computation. By default, the ground truth mesh is required to compute the objective functions, which limits its applicability. In order to remediate this, we proposed a Deep Neural Network, **SOARNet** to infer the respective objective scores for the poses visited so far, $\hat{C} = \{\hat{c}_k : k \leq n\}$ and a further unvisited pose, c_{n+1} given a set of corresponding monocular 2D images up to step n , $\hat{M} = \{m_k : k \leq n\}$, with constraint $n + 1 \leq \mathcal{B}$, and the aforementioned camera parameters of each image; note that our method does not require the image of the unvisited camera-pose as input. Formally,

$$\text{SOARNet}(\hat{C}, \hat{M}, c_{n+1}) = \{\mathbf{F}_g : g \in \{n, n+1\}\} \quad (16)$$

where

$$\mathbf{F}_g = \{f_C^g, f_Q^g, f_D^g, f_T^g\} \quad (17)$$

At each step, the elements of \mathbf{F}_n correspond to the normalized cumulative scores of all poses seen so far for the corresponding objectives. Likewise, \mathbf{F}_{n+1} returns the normalized cumulative scores from an unseen camera-pose, c_{n+1} conditioned upon the visited poses.

The architecture of the model can be found in Fig. 3, where $\mu(\cdot)$ is a ResNet [17] encoder, $o(\cdot)$ is an MLP encoder taking positionally encoded camera extrinsics, and $G(\cdot)$ and $H(\cdot)$ are simple MLP based prediction heads for generating the corresponding objective scores, \mathbf{F}_g via regression. For loss functions, we used the Huber loss on the predictions of each head and take their sum as the final loss, \mathcal{L} as follows

$$\mathcal{L} = \mathcal{L}_G(\hat{\mathbf{F}}_n, \mathbf{F}_n) + \mathcal{L}_H(\hat{\mathbf{F}}_{n+1}, \mathbf{F}_{n+1}) \quad (18)$$

3.3. Trajectory Generation with SOARNet

Once we are able to determine the importance of each candidate pose, the next step would be constructing an optimal trajectory. We propose a simple yet effective greedy strategy by picking the view that maximizes the desired objective at each step. At once, another question naturally follows from the proposed approach, which objective function should be optimized for? We observed that the optimal objective function, is class-dependent - some object classes are better addressed by surface coverage, \mathbf{C} and some via textural complexity, \mathbf{T} instead. Intuitively, this makes sense since each object may physically and visually differ significantly. Therefore, if we simply maximize the total objective scores, it may not actually be picking the candidate with the maximal marginal score of the most effective objective function for the object.

Hence, our trajectory planning algorithm maximizes only a single objective per step in an interleaved manner. This way, we are able to generate a trajectory that accounts for all objectives as a whole. From our empirical testing, we

Algorithm 1 Trajectory Planning

```
1: procedure GENERATETRAJECTORY
2:    $B \leftarrow$  length of budget
3:    $\mathcal{P} \leftarrow$  objective sequence, [C, Q, Q, D, D, T]
4:    $\mathcal{C}^- \leftarrow$  set of unseen poses
5:    $\hat{\mathcal{C}} \leftarrow$  camera poses list
6:    $\hat{\mathcal{M}} \leftarrow$  images list
7:    $n_{\text{init}} \leftarrow$  number of initialization steps
8:   while step  $\leq B$  do
9:     if step  $\leq n_{\text{init}}$  then
10:      do PseudoCoverage
11:     else
12:        $idx \leftarrow \text{step} \% \text{len}(\mathcal{P})$ 
13:       objective,  $f \leftarrow \mathcal{P}[idx]$ 
14:       scores  $\leftarrow$  empty array
15:       for  $c_z$  in  $\mathcal{C}^-$  do
16:          $s_f \xleftarrow{\text{select}f}$  SOARNet  $(\hat{\mathcal{C}}, \hat{\mathcal{M}}, c_z)$ 
17:         scores.append( $s_f$ )
18:        $\hat{\mathcal{C}}.append(\text{argmax}(\text{scores}))$ 
19:       update  $\hat{\mathcal{M}}$ 
20:       step  $\leftarrow$  step + 1
21:   done
```

have found that **D** and **Q** to be most helpful, and therefore we gave particular emphasis to these objectives in our ensemble with the following sequence, [C, Q, Q, D, D, T]; for brevity, we refer to this as the ensemble objective, **E**.

Finally, we hypothesize and indeed observe that having good coverage is of particular importance during initialization when available information is minimal. As such, we utilize an effective yet easy-to-compute pseudo-coverage initialization schema which simply picks poses at the extremum along each principal spatial axis for n_{init} number of poses to begin with. Succinctly, the trajectory planning schema for **E** is summarized in Algorithm 1 with $n_{\text{init}} = 3$.

4. Experiment

In this section, we first present our experimental dataset and setup in Sec. 4.1, before delving more into the results with respect to various baselines in Sec.4.2.

4.1. Dataset and Setup

Dataset. For our experiments, we have created a diverse dataset of 640 objects across 20 classes based on the Objaverse [7] dataset containing Large Vocabulary Instance Segmentation categories [15]. Similar to NeRF-Synthetic [29], for each object we sample images taken from random poses on a fixed-size spherical surface looking inward towards the object, with 100 images for training, 100 for validation and 200 for testing using Blender. More information on the generation process can be found in supplementary.

From this set of objects, we manually computed the individual f_C , f_Q , f_D , and f_T objectives’ score, and generated corresponding trajectories of length 30 via a random walk on the full train-set. Our final train, validation, and test sets have approximately 31k, 1.1k, and 5k samples respectively. For the final evaluation with actual radiance fields training, we further selected a subset of 50 objects from the test set to do so for computational feasibility; this subset will be referred to as the *final-set* for brevity. Finally, we also leveraged the NeRF-Synthetic dataset for out-of-distribution performance test.

Modelling Radiance Fields. For radiance fields modeling, we utilized TensorRF [6] as our primary model. TensorRF adopts a hybrid approach to neural radiance fields modeling unlike the Vanilla NeRF, which enables it to achieve significant speed-up in model training and convergence via tensor decomposition. However, since the proposed objective functions are agnostic with respect to the radiance fields modeling method, we hypothesized that it should be effective regardless of the variants. Indeed, we show that our method generalizes across radiance fields model variants in Sec. 4.2.

Experimental Setup. The SOARNet model was trained on a machine with an NVIDIA RTX8000 GPU, 64GB of DRAM and 8 CPUs. The model was trained with a step-scheduler of step size of 0.6 and γ of 0.5, and the Adam optimizer [23] at a learning rate of $3e-5$, β_1 of 0.9 and β_2 of 0.999, ϵ of $1e-08$, with AMSGrad [36] enabled, and no weight decay. Finally, we trained the model for 12 epochs with a batch-size of 8.

We leverage the NerfStudio [40] implementations of TensorRF [6] and Vanilla-NeRF [29] for radiance field training. We also use Plenoxels [10] and ActiveNeRF [33] provided by the respective authors. For details on the exact configurations, please refer to supplementary.

4.2. Results Evaluation

Primary Evaluation. We first evaluate the performance of our model on the NeRF-Synthetic dataset with unseen classes and objects of higher complexity for a challenging out-of-distribution test. Note that *chair* has been removed from the evaluation since our original training dataset contains said class. The result can be found in Tab. 1. For this evaluation, we compare our performance against a prior approach, ActiveNeRF [33]. Additionally, we have also trained multiple instances of each object across a range of budget, with $\mathcal{B} \in \{3, 6, 12, 20, 30\}$. This way, we should be able to get a better representation of the potency of each method. We reported the averaged result across said budgets on 3 reconstruction metrics of Peak Signal-to-Noise Ratio (PSNR), Structural Similarity Index Measure (SSIM)

Object	PSNR (\uparrow)		LPIPS (\downarrow)		SSIM (\uparrow)		Time (\downarrow)			
	AN	Ours	AN	Ours	AN	Ours	AN (TG)	AN (RFT)	Ours (TG)	Ours (RFT)
drums	17.92	18.25	0.332	0.322	0.779	0.774	14h 12m		20s	11m 42s
ficus	21.55	21.81	0.169	0.163	0.869	0.877	14h 18m		20s	15m 6s
hotdog	25.36	28.77	0.202	0.123	0.888	0.921	14h 10m		20s	10m 13s
lego	23.57	25.17	0.169	0.127	0.835	0.865	14h 12m		20s	9m 46s
materials	19.54	21.27	0.234	0.192	0.811	0.839	14h 22m		20s	10m 4s
mic	24.66	24.94	0.146	0.135	0.913	0.918	14h 14m		20s	8m 36s
ship	21.27	21.14	0.334	0.332	0.721	0.716	14h 17m		20s	11m 28s

Table 1. Reconstruction quality of **TensorRF** [6] trained via trajectory generated **ActiveNeRF**, **AN** [33] and **Ensemble** (Ours) on NeRF Synthetic. For time, **TG** is the trajectory generation time, and **RFT** is the radiance fields training time. Best result is represented with **bold**.

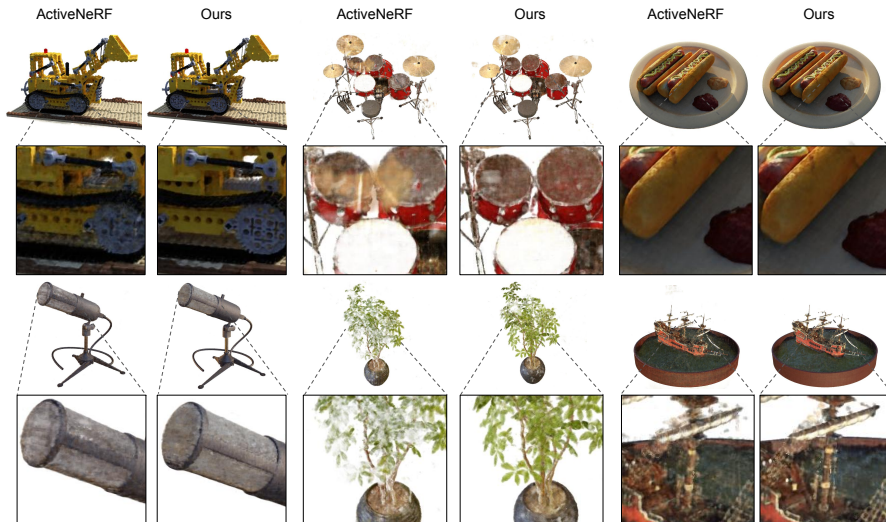


Figure 4. Example renders with our method against the baseline, ActiveNeRF. Here we used a budget of $B = 30$ for all instances.

[42] and Perceptual Similarity (LPIPS) [48].

Firstly, note that the reconstruction quality of a model trained via our Ensemble schema, **E** outperforms ActiveNeRF in almost every class and across all reconstruction quality metrics, lagging behind only on *ship* by a small margin, demonstrating its potency. Secondly, since our proposed approach is model agnostic for radiance fields modeling, we can therefore decouple trajectory planning from the radiance fields training. Succinctly, this means, unlike [33, 35] where they are locked into a particular radiance fields model, which could be very slow to train, our approach does not impose such a restriction and does not require any radiance fields training for trajectory planning. For these reasons, we are able to achieve a significant speed-up, with an average $\sim 80x$ improvement compared to the ActiveNeRF. In Tab. 1 we report the total time taken as two separate components - the *trajectory generation* time, TG and the *radiance fields training* time, RFT. For ActiveNeRF we report only a single value for both time components since the two processes are inherently one. Finally, we re-

trained additional TensorRF instances with the trajectories generated via ActiveNeRF with the same configurations so the reconstruction metrics would be comparable; for fairness, we have omitted the time taken for said retraining. It should be noted that our approach does not need the image taken from a candidate unseen pose for scoring, only the camera extrinsics, rendering it much more useful in real-world applications (e.g. does not need tedious sampling by actual visitation of poses). Renders of sample views of the methods can be found in Fig. 4 for visual comparison.

For the in-distribution evaluation, we trained TensorRF on the custom Objaverse final-set via 6 trajectory planning schemas - **Random** as a baseline, **Ensemble** as described in Sec. 3.3, and the maximization of **individual objective functions** f_C , f_Q , f_D and f_D . For the random baseline, we independently generated 5 trajectories per object and reported their averaged result. As mentioned prior, the optimal objective function could differ across objects based on their physical representation. As such, we have grouped the set of results trained on the trajectory generated via the *in-*

Object	Vanilla NeRF						Plenoxels					
	PSNR (\uparrow)		LPIPS (\downarrow)		SSIM (\uparrow)		PSNR (\uparrow)		LPIPS (\downarrow)		SSIM (\uparrow)	
	Rand	Ours	Rand	Ours	Rand	Ours	Rand	Ours	Rand	Ours	Rand	Ours
bookcase	33.83	35.02	0.042	0.038	0.975	0.979	25.32	26.67	0.123	0.107	0.927	0.940
cone	31.50	31.75	0.059	0.055	0.969	0.970	–	–	–	–	–	–
earphone	30.94	31.74	0.029	0.023	0.974	0.977	26.10	27.41	0.098	0.084	0.940	0.947
globe	28.83	28.52	0.039	0.043	0.958	0.955	23.89	23.61	0.129	0.131	0.916	0.911
shoe	26.31	26.82	0.054	0.050	0.950	0.952	–	–	–	–	–	–
snowman	35.63	36.93	0.017	0.014	0.991	0.993	31.87	33.24	0.049	0.050	0.977	0.978

Table 2. Reconstruction quality of **Vanilla NeRF** [29] and **Plenoxels** [10] trained via trajectories generated from **Ensemble** (Ours) against the **Random** baseline. Results here are based on a subset of 6 objects from our Objaverse test-set and averaged across a range of budgets. The best result is represented with **bold**.

Method	PSNR (\uparrow)	LPIPS (\downarrow)	SSIM (\uparrow)
Random	29.07	0.081	0.951
E (Ours)	<u>29.45</u>	<u>0.071</u>	<u>0.955</u>
OP (Ours)	29.67	0.068	0.957

Table 3. Averaged result of **Optimal CQDT**, **OP** and **Ensemble**, **E** against the **Random** baseline. The best result is represented with **bold**, and second best with underline.

dividual objective functions and took the best performing amongst them as another candidate schema dubbed, **Optimal CQDT**. The results can be found in Tab. 3; we used a simple baseline here due to limited computational resource.

From the table, we can observe that Optimal CQDT performs the best, with Ensemble coming in as the second best, outperforming the Random baselines. The superior performance of Optimal CQDT reveals that the objects from the Objaverse dataset can be saliently captured and represented by a single objective function. However, it should also be noted that the efficacy may not be homogeneous across the objective functions for a given object. For example, for *bookcase*, f_D is worse than f_C . We hypothesized that this is due to the complexity of the shelving and large-flat surfaces, which creates a local minima for f_D , resulting in an over concentration around a local region. On the flip side, for *soccer.ball*, the random baseline is actually competitive compared to the other schemas. We hypothesized that for objects that are geometrically simple and easily covered from all directions, random walk could suffice since the difference in saliency across poses is minimal. From this observation, we further hypothesized that for such objects, one could simply utilize a cheap random walk for trajectory planning. The breakdown of the result by class can be found in the supplementary.

Lastly, Ensemble does indeed offer a viable alternative to trajectory planning when the optimal objective function

is not known ahead of time, or if it’s too costly to be determined explicitly.

Model Variant Generalization. Intuitively, our approach should also generalize across radiance field model variants since the objective functions are grounded in geometry and photometric visual cues. Therefore, we also tested for such generalization by evaluating the approach on a subset of our Objaverse dataset with a fully neural-implicit radiance fields model, Vanilla NeRF and a fully explicit model, Plenoxels. With these, our evaluations covered the spectrum of radiance fields models from fully neural-implicit to fully explicit models. The result of the evaluation can be found in Tab. 2. For the results on *cone* and *shoe* with Plenoxels, we have omitted them as Plenoxels is unable to converge for them at all. The result validates our hypothesis by demonstrating that indeed, the proposed schema remain efficacious across model variants in almost all cases.

5. Conclusion

Limitation. The current ensembling schema is quite simple and by no means exhaustive; our future studies will consider more effective ways to merge the proposed objective functions. Additionally, we currently focus only on inward-looking scenes with singular objects, which is not representative of the complex environment one may encounter in complex mapping and navigation tasks. Therefore, we would also like to apply SOAR to more challenging large-scale environments in future works.

Summary. In this work, we have proposed SOAR, a set of objective functions designed to serve as surrogates to indicate the goodness of a resultant radiance fields model, given a set of inputs. In order to enable efficient inference for real-time trajectory generation, we further proposed a deep neural network, SOARNet that enables per-step planning in $<1s$ on unseen poses. With extensive evaluations, we have shown that indeed our approach is

able to outperform various baselines, even in challenging out-of-distribution scenarios and across radiance fields model variants.

Acknowledgement We extend our gratitude to several individuals and teams whose support contributed to the fruition of our work. We express our appreciation to Mohit Mehta and Anbang Yang for their helpful discussion, and to the NYU High Performance Computing team for their support in our experimentation. The work is supported by NSF Awards 2238968 and 2322242.

References

- [1] Relja Arandjelović and Andrew Zisserman. Nerf in detail: Learning to sample for view synthesis. *arXiv preprint arXiv:2106.05264*, 2021. 2
- [2] R. Bajcsy. Active perception. *Proceedings of the IEEE*, 76(8):966–1005, 1988. 1, 2
- [3] Ruzena Bajcsy, Yiannis Aloimonos, and John K Tsotsos. Re-visiting active perception. *Autonomous Robots*, 42:177–196, 2018. 2
- [4] Eric R Chan, Koki Nagano, Matthew A Chan, Alexander W Bergman, Jeong Joon Park, Axel Levy, Miika Aittala, Shalini De Mello, Tero Karras, and Gordon Wetzstein. Generative novel view synthesis with 3d-aware diffusion models. *arXiv preprint arXiv:2304.02602*, 2023. 2
- [5] Anpei Chen, Zexiang Xu, Fuqiang Zhao, Xiaoshuai Zhang, Fanbo Xiang, Jingyi Yu, and Hao Su. Mvsnerf: Fast generalizable radiance field reconstruction from multi-view stereo. In *Proceedings of the IEEE/CVF International Conference on Computer Vision*, pages 14124–14133, 2021. 2
- [6] Anpei Chen, Zexiang Xu, Andreas Geiger, Jingyi Yu, and Hao Su. Tensorf: Tensorial radiance fields. In *European Conference on Computer Vision (ECCV)*, 2022. 2, 6, 7, 1
- [7] Matt Deitke, Dustin Schwenk, Jordi Salvador, Luca Weihs, Oscar Michel, Eli VanderBilt, Ludwig Schmidt, Kiana Ehsani, Aniruddha Kembhavi, and Ali Farhadi. Objaverse: A universe of annotated 3d objects. In *Proceedings of the IEEE/CVF Conference on Computer Vision and Pattern Recognition*, pages 13142–13153, 2023. 6, 1
- [8] Nianchen Deng, Zhenyi He, Jiannan Ye, Budmonde Duinkharjav, Praneeth Chakravarthula, Xubo Yang, and Qi Sun. Fov-nerf: Foveated neural radiance fields for virtual reality. *IEEE Transactions on Visualization and Computer Graphics*, 28(11):3854–3864, 2022. 2
- [9] Harnaik Dhami, Vishnu D Sharma, and Pratap Tokekar. Pred-nbv: Prediction-guided next-best-view for 3d object reconstruction. *arXiv preprint arXiv:2304.11465*, 2023. 2
- [10] Sara Fridovich-Keil, Alex Yu, Matthew Tancik, Qinhong Chen, Benjamin Recht, and Angjoo Kanazawa. Plenoxels: Radiance fields without neural networks. In *Proceedings of the IEEE/CVF Conference on Computer Vision and Pattern Recognition (CVPR)*, pages 5501–5510, 2022. 2, 6, 8, 1
- [11] Kyle Gao, Yina Gao, Hongjie He, Dening Lu, Linlin Xu, and Jonathan Li. Nerf: Neural radiance field in 3d vision, a comprehensive review. *arXiv preprint arXiv:2210.00379*, 2022. 2
- [12] Stephan J Garbin, Marek Kowalski, Matthew Johnson, Jamie Shotton, and Julien Valentin. Fastnerf: High-fidelity neural rendering at 200fps. In *Proceedings of the IEEE/CVF International Conference on Computer Vision*, pages 14346–14355, 2021. 2
- [13] Lily Goli, Cody Reading, Silvia Sellán, Alec Jacobson, and Andrea Tagliasacchi. Bayes’ rays: Uncertainty quantification for neural radiance fields. *arXiv preprint arXiv:2309.03185*, 2023. 2, 3
- [14] Antoine Guédon, Pascal Monasse, and Vincent Lepetit. Scone: Surface coverage optimization in unknown environments by volumetric integration. *Advances in Neural Information Processing Systems*, 35:20731–20743, 2022. 2
- [15] Agrim Gupta, Piotr Dollar, and Ross Girshick. Lvis: A dataset for large vocabulary instance segmentation. In *Proceedings of the IEEE/CVF conference on computer vision and pattern recognition*, pages 5356–5364, 2019. 6, 1
- [16] Antoine Guédon, Tom Monnier, Pascal Monasse, and Vincent Lepetit. MACARONS: Mapping And Coverage Anticipation with RGB ONline Self-supervision. In *CVPR*, 2023. 2
- [17] Kaiming He, Xiangyu Zhang, Shaoqing Ren, and Jian Sun. Deep residual learning for image recognition. In *Proceedings of the IEEE conference on computer vision and pattern recognition*, pages 770–778, 2016. 5
- [18] Peter Hedman, Pratul P. Srinivasan, Ben Mildenhall, Jonathan T. Barron, and Paul Debevec. Baking neural radiance fields for real-time view synthesis. *ICCV*, 2021. 2
- [19] Ajay Jain, Matthew Tancik, and Pieter Abbeel. Putting nerf on a diet: Semantically consistent few-shot view synthesis. In *Proceedings of the IEEE/CVF International Conference on Computer Vision*, pages 5885–5894, 2021. 2
- [20] Chenxing Jiang, Hanwen Zhang, Peize Liu, Zehuan Yu, Hui Cheng, Boyu Zhou, and Shaojie Shen. H₂-mapping: Real-time dense mapping using hierarchical hybrid representation. *IEEE Robotics and Automation Letters*, 8(10):6787–6794, 2023. 2
- [21] Liren Jin, Xieyuanli Chen, Julius Rücker, and Marija Popović. Neu-nbv: Next best view planning using uncertainty estimation in image-based neural rendering. In *2023 IEEE/RSJ International Conference on Intelligent Robots and Systems (IROS)*, 2023. 2, 3
- [22] Bernhard Kerbl, Georgios Kopanas, Thomas Leimkühler, and George Drettakis. 3d gaussian splatting for real-time radiance field rendering. *ACM Transactions on Graphics*, 42(4), 2023. 2
- [23] Diederik P Kingma and Jimmy Ba. Adam: A method for stochastic optimization. *arXiv preprint arXiv:1412.6980*, 2014. 6
- [24] Georgios Kopanas and George Drettakis. Improving NeRF Quality by Progressive Camera Placement for Free-Viewpoint Navigation. In *Vision, Modeling, and Visualization*. The Eurographics Association, 2023. 2
- [25] Soomin Lee, Chen Le, Wang Jiahao, Alexander Liniger, Suryansh Kumar, and Fisher Yu. Uncertainty guided pol-

- icy for active robotic 3d reconstruction using neural radiance fields. *IEEE Robotics and Automation Letters*, 2022. [3](#)
- [26] Ke Li, Tim Rolff, Susanne Schmidt, Reinhard Bacher, Wim Leemans, and Frank Steinicke. Interacting with neural radiance fields in immersive virtual reality. In *Extended Abstracts of the 2023 CHI Conference on Human Factors in Computing Systems*, New York, NY, USA, 2023. Association for Computing Machinery. [2](#)
- [27] Yuan Liu, Sida Peng, Lingjie Liu, Qianqian Wang, Peng Wang, Christian Theobalt, Xiaowei Zhou, and Wenping Wang. Neural rays for occlusion-aware image-based rendering. In *Proceedings of the IEEE/CVF Conference on Computer Vision and Pattern Recognition*, pages 7824–7833, 2022. [2](#)
- [28] Yu-Lun Liu, Chen Gao, Andreas Meuleman, Hung-Yu Tseng, Ayush Saraf, Changil Kim, Yung-Yu Chuang, Johannes Kopf, and Jia-Bin Huang. Robust dynamic radiance fields. In *Proceedings of the IEEE/CVF Conference on Computer Vision and Pattern Recognition*, 2023. [2](#)
- [29] Ben Mildenhall, Pratul P. Srinivasan, Matthew Tancik, Jonathan T. Barron, Ravi Ramamoorthi, and Ren Ng. Nerf: Representing scenes as neural radiance fields for view synthesis. In *ECCV*, 2020. [2](#), [6](#), [8](#), [1](#)
- [30] Thomas Müller, Alex Evans, Christoph Schied, and Alexander Keller. Instant neural graphics primitives with a multiresolution hash encoding. *ACM Trans. Graph.*, 41(4):102:1–102:15, 2022. [2](#)
- [31] Tonci Novkovic, Remi Pautrat, Fadri Furrer, Michel Breyer, Roland Siegwart, and Juan Nieto. Object finding in cluttered scenes using interactive perception. In *2020 IEEE International Conference on Robotics and Automation (ICRA)*, pages 8338–8344. IEEE, 2020. [2](#)
- [32] T. Ojala, M. Pietikainen, and T. Maenpaa. Multiresolution gray-scale and rotation invariant texture classification with local binary patterns. *IEEE Transactions on Pattern Analysis and Machine Intelligence*, 24(7):971–987, 2002. [4](#)
- [33] Xuran Pan, Zihang Lai, Shiji Song, and Gao Huang. Activenerf: Learning where to see with uncertainty estimation. In *Computer Vision—ECCV 2022: 17th European Conference, Tel Aviv, Israel, October 23–27, 2022, Proceedings, Part XXXIII*, pages 230–246. Springer, 2022. [1](#), [2](#), [3](#), [6](#), [7](#)
- [34] R. Pito. A solution to the next best view problem for automated surface acquisition. *IEEE Transactions on Pattern Analysis and Machine Intelligence*, 21(10):1016–1030, 1999. [2](#)
- [35] Yunlong Ran, Jing Zeng, Shibo He, Jiming Chen, Lincheng Li, Yingfeng Chen, Gimhee Lee, and Qi Ye. Neurar: Neural uncertainty for autonomous 3d reconstruction with implicit neural representations. *IEEE Robotics and Automation Letters*, 8(2):1125–1132, 2023. [2](#), [3](#), [7](#)
- [36] Sashank J. Reddi, Satyen Kale, and Sanjiv Kumar. On the convergence of adam and beyond. In *International Conference on Learning Representations*, 2018. [6](#)
- [37] Xinyi Ren, Jianlan Luo, Eugen Solowjow, Juan Aparicio Ojea, Abhishek Gupta, Aviv Tamar, and Pieter Abbeel. Domain randomization for active pose estimation. In *2019 International Conference on Robotics and Automation (ICRA)*, pages 7228–7234. IEEE, 2019. [2](#)
- [38] Antoni Rosinol, John J Leonard, and Luca Carlone. Nerfslam: Real-time dense monocular slam with neural radiance fields. *arXiv preprint arXiv:2210.13641*, 2022. [2](#)
- [39] Jianxiong Shen, Adria Ruiz, Antonio Agudo, and Francesc Moreno-Noguer. Stochastic neural radiance fields: Quantifying uncertainty in implicit 3d representations. In *2021 International Conference on 3D Vision (3DV)*, pages 972–981. IEEE, 2021. [3](#)
- [40] Matthew Tancik, Ethan Weber, Evonne Ng, Ruilong Li, Brent Yi, Justin Kerr, Terrance Wang, Alexander Kristoffersen, Jake Austin, Kamyar Salahi, Abhik Ahuja, David McAllister, and Angjoo Kanazawa. Nerfstudio: A modular framework for neural radiance field development. In *ACM SIGGRAPH 2023 Conference Proceedings*, 2023. [6](#), [1](#)
- [41] Tsun-Hsuan Wang, Sivabalan Manivasagam, Ming Liang, Bin Yang, Wenyuan Zeng, and Raquel Urtasun. V2vnet: Vehicle-to-vehicle communication for joint perception and prediction. In *Computer Vision—ECCV 2020: 16th European Conference, Glasgow, UK, August 23–28, 2020, Proceedings, Part II 16*, pages 605–621. Springer, 2020. [2](#)
- [42] Zhou Wang, Alan C Bovik, Hamid R Sheikh, and Eero P Simoncelli. Image quality assessment: from error visibility to structural similarity. *IEEE transactions on image processing*, 13(4):600–612, 2004. [7](#)
- [43] Jamie Wynn and Daniyar Turmukhambetov. DiffusioNeRF: Regularizing Neural Radiance Fields with Denoising Diffusion Models. In *CVPR*, 2023. [2](#)
- [44] Linning Xu, Vasu Agrawal, William Laney, Tony Garcia, Aayush Bansal, Changil Kim, Samuel Rota Bulò, Lorenzo Porzi, Peter Kotschieder, Aljaž Božič, Dahua Lin, Michael Zollhöfer, and Christian Richardt. VR-NeRF: High-fidelity virtualized walkable spaces. In *SIGGRAPH Asia Conference Proceedings*, 2023. [2](#)
- [45] Alex Yu, Vickie Ye, Matthew Tancik, and Angjoo Kanazawa. pixelnerf: Neural radiance fields from one or few images. In *Proceedings of the IEEE/CVF Conference on Computer Vision and Pattern Recognition*, pages 4578–4587, 2021. [2](#)
- [46] Jason J. Yu, Fereshteh Forghani, Konstantinos G. Derpanis, and Marcus A. Brubaker. Long-term photometric consistent novel view synthesis with diffusion models. In *Proceedings of the International Conference on Computer Vision (ICCV)*, 2023. [2](#)
- [47] Rui Zeng, Wang Zhao, and Yong-Jin Liu. Pc-nbv: A point cloud based deep network for efficient next best view planning. In *2020 IEEE/RSJ International Conference on Intelligent Robots and Systems (IROS)*, pages 7050–7057. IEEE, 2020. [2](#)
- [48] Richard Zhang, Phillip Isola, Alexei A Efros, Eli Shechtman, and Oliver Wang. The unreasonable effectiveness of deep features as a perceptual metric. In *Proceedings of the IEEE conference on computer vision and pattern recognition*, pages 586–595, 2018. [7](#)
- [49] Chengxuan Zhu, Renjie Wan, Yunkai Tang, and Boxin Shi. Occlusion-free scene recovery via neural radiance fields. In *Proceedings of the IEEE/CVF Conference on Computer Vision and Pattern Recognition (CVPR)*, pages 20722–20731, 2023. [2](#)

- [50] Zihan Zhu, Songyou Peng, Viktor Larsson, Weiwei Xu, Hujun Bao, Zhaopeng Cui, Martin R. Oswald, and Marc Pollefeys. Nice-slam: Neural implicit scalable encoding for slam. In *Proceedings of the IEEE/CVF Conference on Computer Vision and Pattern Recognition (CVPR)*, 2022. [2](#)

SO-NeRF: Active View Planning for NeRF using Surrogate Objectives

Supplementary Material

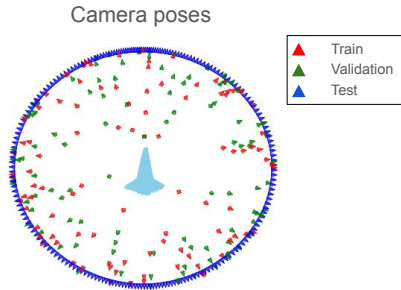


Figure 5. Visualization of the camera poses visited to sample views for the train, validation and test sets of the *cone* object.

6. Supplementary

As supplementary, we provided more details of our proposed approach below. In Sec. 6.1, we discuss about the dataset generation procedure used to generate our custom Objaverse [7] based dataset. Then in Sec. 6.2 we outlined the detailed configurations we used for the respective radiance fields model and baseline. Thereafter in Sec. 6.3, a further drill-down of the results previously shown in Tab. 3 of Sec. 4.2 is provided. Finally, we provided a video visualizing the trajectories and resulting novel view synthesis renders of our method, SO-NeRF against ActiveNeRF [33] in Sec. 6.4.

6.1. Dataset Generation

To begin, we generated our custom dataset using the Objaverse API [7]. Given the large variety of classes and object instances per class that are available within the Objaverse dataset, there is an expected amount of noise to the labels. For this reason, we specifically select only Large Vocabulary Instance Segmentation [15] (LVIS) objects within Objaverse, which have been manually verified by humans.

Just like the NeRF Synthetic dataset, our custom data generation procedure samples views from poses around the object constrained to a fixed radius; this is equivalent to sampling views from the surface of an imaginary sphere. For the training and validation set, we performed the sampling randomly around the object, whereas for the test set, we used a smooth circular trajectory instead for ease of viewing. An illustration of the aforementioned sampling procedures can be found in Fig. 5. The procedure is summarized in Algorithm 2. We ran the algorithm on a machine with a single AMD Radeon MI50 GPU, 4 CPUs and 16GB of DRAM.

Overall, we sampled 640 objects across 20 classes - specifically, *bookcase*, *chair*, *cone*, *control*, *die*, *earphone*,

Algorithm 2 ProcessGLB

```
1: procedure PROCESSGLB
2:   CLEANSCENE()           ▷ Clean the blender scene
3:    $obj \leftarrow$  LOADOBJECT( $glb\_file\_path$ )
4:   SCALEOBJECT( $obj$ )      ▷ Normalize scale
5:    $imgs, cam\_parameters \leftarrow$  SAMPLEVIEWS()
6:   SAVEOBJ( $obj$ )          ▷ Export obj + mtl file
7:   SAVESAMPLES( $imgs, cam\_parameters$ )
```

fan, *fireplug*, *fighter_jet*, *globe*, *gravestone*, *guitar*, *lion*, *shoe*, *snowman*, *soccer_ball*, *sunglasses*, *teddybear*, *toilet*, and *vase* from the list of available categories. For each class, we downloaded twenty instances of that class and manually verified the labels for reliability. We pruned or replaced any outlier objects. Visualizations of the object classes can be found in Fig. 6.

6.2. Additional Model Configuration Details

For radiance fields modeling, we leveraged the Nerfstudio [40] implementations of TensorRF [6] and Vanilla NeRF [29] for training. For TensorRF, we trained each object-instance for 300 epochs with all other configurations left as default. For Vanilla NeRF, we trained each object-instance for 3,000 epochs instead for better convergence, with all other configurations left as default as well. For Plenoxels [10], we trained it with an epoch-size of 300 per object, with a learning rate of $3e1$, and spherical harmonics learning rate of $1e-2$ with all other configurations as default. In terms of hardware, both models were trained on a platform with an NVIDIA RTX8000 GPU, 32GB of DRAM, and 2 CPUs.

For our ActiveNeRF baseline, all the trajectory planning and generation runs were conducted on a machine with an NVIDIA RTX8000 GPU, 64GB of system DRAM, and 8 CPUs for training, per object. We initialized each instance with a seed training set with 5 poses and let ActiveNeRF determine the required remaining images based on the quantified uncertainty. Closely following the experimental configuration of [33], we trained the model for 200,000 iterations each, and let it pick the remaining $B - 5$ number of images over the course of those iterations at a cadence of 5 images per 40,000 steps and minimum uncertainty kept at 0.01. The remaining settings were all kept at default.

6.3. Additional Result Breakdown

In Sec. 4.2, the averaged results on the Objaverse dataset were reported in Tab. 3. In this section, we go one step further by breaking down the result per-class to provide better

Class	PSNR (\uparrow)			LPIPS (\downarrow)			SSIM (\uparrow)		
	Rand	E	Op. CQDT	Rand	E	Op. CQDT	Rand	E	Op. CQDT
bookcase	28.94	30.37	30.42	0.089	0.078	0.074	0.946	0.956	0.957
chair	29.33	29.59	30.00	0.084	0.069	0.067	0.949	0.956	0.957
cone	27.64	28.37	28.59	0.100	0.088	0.083	0.938	0.945	0.947
control	29.33	30.41	30.48	0.069	0.055	0.055	0.957	0.965	0.965
earphone	29.16	29.74	30.05	0.074	0.060	0.058	0.954	0.961	0.961
fan	27.30	27.01	26.98	0.091	0.092	0.093	0.939	0.938	0.938
fireplug	30.21	30.37	31.30	0.064	0.065	0.054	0.959	0.959	0.964
globe	25.54	26.05	26.14	0.110	0.094	0.089	0.915	0.925	0.928
gravestone	31.43	31.52	31.59	0.054	0.050	0.051	0.967	0.968	0.969
guitar	32.22	32.43	32.33	0.053	0.045	0.045	0.976	0.979	0.979
lion	30.53	30.70	30.57	0.063	0.053	0.052	0.962	0.965	0.965
shoe	26.23	26.97	26.73	0.099	0.085	0.085	0.931	0.937	0.937
snowman	32.01	32.49	32.62	0.063	0.057	0.056	0.966	0.970	0.971
soccer_ball	25.53	24.24	25.10	0.113	0.109	0.097	0.941	0.939	0.944
sunglasses	28.26	28.01	28.61	0.093	0.079	0.072	0.955	0.958	0.962
teddy_bear	30.92	31.44	31.53	0.064	0.055	0.054	0.960	0.965	0.965
toilet	28.95	29.53	30.13	0.098	0.086	0.077	0.943	0.950	0.954
vase	29.75	30.92	30.97	0.073	0.063	0.064	0.952	0.959	0.959

Table 4. Reconstruction quality of **TensorRF** trained via trajectory generated from **Optimal CQDT** and **Ensemble, E** against the **Random** baseline. Results here are grouped by object class and averaged across the budgets. The best result is represented with **bold**.



Figure 6. Preview of an object from each class of our custom Objaverse dataset used to train and evaluate SOARNet.

clarity on the performance of our proposed approach - **Ensemble** and **Optimal CQDT** as previously defined - against the **Random** baseline in Tab. 4.

As we can observe from the table, the proposed approaches worked the best in almost all cases, except for *soccer_ball* and *fan*, across all 3 metrics. The results shown here affirm the findings and conclusion we put forth previously.

6.4. Video Rendering

For additional visualization and demonstration of our approach, we have included a short video together with the supplementary submission to illustrate the trajectory generated and test-set renderings of SO-NeRF against ActiveNeRF on the NeRF Synthetic dataset.